

Hollow multi-shelled NiO nanoreactor for nanoconfined catalytic degradation of organic pollutants via peroxydisulfate activation

Gen Wang^a, Ke Wang^a, Zhuoyue Liu^a, Youyou Feng^b, Shengjiong Yang^a, Yaqiong Su^c, Xufang Qian^{d,*}, Pengkang Jin^{a,*}, Jing Wei^{b,*}

^a School of Environmental and Municipal Engineering, Xi'an University of Architecture and Technology, Xi'an, Shaanxi 710055, PR China

^b The Key Laboratory of Biomedical Information Engineering of Ministry of Education, School of Life Science and Technology, Xi'an Jiaotong University, Xi'an, Shaanxi 710049, PR China

^c School of Chemistry, Xi'an Key Laboratory of Sustainable Energy Materials Chemistry, State Key Laboratory of Electrical Insulation and Power Equipment, Xi'an Jiaotong University, Xi'an, Shaanxi 710049, PR China

^d School of Environmental Science and Engineering, Shanghai Jiao Tong University, Shanghai 200240, China; Shanghai Institute of Pollution Control and Ecological Security, Shanghai 200092, PR China



ARTICLE INFO

Keywords:

Hollow multi-shelled structure
NiO
Nanoconfinement effect
Peroxydisulfate
Electron transfer process

ABSTRACT

Nonradical activation of peroxydisulfate (PDS) is promising for wastewater decontamination but suffers from insufficient decomposition efficiency toward organics. Herein, NiO nanospheres with hollow multi-shelled structure (HoMS) and tunable shell numbers are designed as a nanoreactor of PDS activation to enhance the decomposition efficiency. Study on bis-phenol A (BPA) degradation reveals that 3-shelled NiO HoMS exhibits enhanced kinetic rate (0.08 min^{-1}) and mineralization degree (79.2%) compared to 2-shelled NiO HoMS (0.04 min^{-1} , 50%) and NiO nanoparticles (0.01 min^{-1} , 29.8%). The degradation of BPA over NiO HoMS follows electron transfer regime with oxygen vacancy (V_O) acted as the active site. The hollow multi-shelled structure not only increases the accessibility of V_O but also enriches local concentration of reactants in the void spaces due to the nanoconfinement effect, and thus mainly contributes to the enhanced catalytic efficiency. This work provides a distinct case for developing efficient nonradical oxidation technique for water purification.

1. Introduction

Water contamination by endocrine disrupting chemicals (EDCs) such as bis-phenol A (BPA) has aroused great concern associated with their adverse effects on ecosystems and public health [1–3]. Advanced oxidation processes (AOPs) based on heterogeneous activation of peroxydisulfate (PDS) is proposed as a promising technique to eliminate EDCs owing to the cost-effectiveness and mild operation conditions [4–7]. Radical oxidation with sulfate radical ($\text{SO}_4^{\cdot-}$) and/or hydroxyl radical ($\cdot\text{OH}$) has been widely studied for EDCs removal, but suffers from poor selectivity and compromised performance in complicated water matrices [8–10]. In recent years, nonradical oxidation based on electron transfer process (ETP) has attracted increasing interests due to the high selectivity and good resistance to complex surroundings like inorganic ions and natural organic matters [11–13]. In ETP-based non-radical oxidation, organics can be readily oxidized at the initial stage [12]. Due to the mild oxidative potential, however, complete

decomposition of organics is challenging and still needs to be improved.

Carbonaceous materials such as carbon nanotube are commonly used to trigger the electron transfer process in PDS activation [14–16]. Recently, transition metal oxides such as NiO were also reported to be able to drive the electron transfer process, and have attracted increasing interests due to their natural abundance and good stability [17,18]. In a heterogeneous oxidation process, the degradation of organic contaminants happens randomly on the surface of metal oxides. The efficiency of organics removal is closely related to the number of active sites [19–21]. Constructing novel structured metal oxides with large number of active sites is a promising approach to enhance the catalytic efficiency. Nanomaterials with hollow multi-shelled structure (HoMS) exhibit large surface area and highly exposed catalytic sites, and thus have been extensively studied recently [22–25]. In a peroxyomonosulfate (PMS)-based oxidation process, for example, the degradation rate of 2-chlorophenol over 3-shelled Co_3O_4 hollow microspheres was determined to be 22 times higher than that over solid Co_3O_4 nanoparticles

* Corresponding authors.

E-mail addresses: qianxufang@sjtu.edu.cn (X. Qian), pkjin@xauat.edu.cn (P. Jin), jingwei@xjtu.edu.cn (J. Wei).

[26]. More importantly, the void space of hollow multi-shelled structure is capable of confining reactants, increasing their instantaneous concentrations and altering their diffusion flux during the catalysis reaction [26–28]. Such nanoconfinement effect could dramatically accelerate the reaction kinetics and thus further enhance the decomposition of organics. For example, Wang et al. reported that the shells of hollow $\text{Co}_3\text{O}_4/\text{NiCo}_2\text{O}_4$ nanocages could increase the instantaneous concentration of reactants in the void space, enabling more efficient degradation of BPA than the nonhollow $\text{Co}_3\text{O}_4/\text{NiCo}_2\text{O}_4$ composite nanoparticles [29]. Based on the nanoconfinement effect of HoMS nanocatalysts, it is conceived that the catalytic efficiency of ETP-based oxidation would be improved by design of HoMS nanocatalysts for PDS activation. Till now, there were very few literatures on metal oxide-based HoMS catalysts for confined catalytic degradation of organics via ETP-based PDS activation.

To enhance the decomposition efficiency of organics in ETP-based PDS activation, surface properties of metal oxide catalysts should be additionally addressed as they greatly affect PDS adsorption and electron transfer efficiency between PDS and organics. Surface defects such as oxygen vacancy (V_O) has been proved to be crucial for PDS activation [30–32]. The presence of V_O enables improved electron accumulation and transportation, and thus led to higher catalytic activity [33,34]. On the other hand, introducing surface V_O could facilitate the adsorption of PDS and formation of surface bonded-PDS complex, which directly interacted with organics to finalize their oxidation [17,18]. Therefore, constructing V_O in HoMS metal oxides is also essential to improve its catalytic efficiency toward PDS activation and organics decomposition.

Herein, hollow structured NiO nanospheres with tunable shell numbers and oxygen vacancy (V_O) contents were prepared via a self-template method using metal-polyphenol coordination polymer (Ni-TA) as the precursor. The NiO HoMS was employed as a nanoreactor of PDS activation, aiming to boost the catalytic efficiency of the ETP-based nonradical oxidation. The degradation of BPA followed an electron transfer regime and the catalytic efficiency was greatly enhanced upon increasing the shell numbers. V_O was proved to be the active site of PDS activation based on spectra analysis and density functional theory (DFT) calculations. The hollow multi-shelled structure not only increased the accessibility of V_O but locally enriched reactants in the void spaces (i.e., nanoconfinement effect), and thus mainly contributed to the enhanced catalytic efficiency. The NiO HoMS nanoreactors exhibited outstanding performance toward organics removal in complex surroundings, e.g., working pH, inorganic ions, natural organic matters and real water matrix, revealing a promising potential for water purification.

2. Experimental section

2.1. Chemicals

$\text{Ni}(\text{NO}_3)_2 \cdot 6 \text{ H}_2\text{O}$, tannic acid (TA), bis-phenol A (BPA) and potassium peroxydisulfate (PDS) were bought from Macklin Biochemical Co., Ltd, China. Methanol (MeOH), tert-butanol (TBA), L-histidine, 5,5-dimethyl-1-pyrolin-Noxide (DMPO), 2,2,6,6-tetramethyl-4-piperidone (TEMP), *p*-benzoquinone (BQ), potassium iodide (KI) and $\text{K}_2\text{Cr}_2\text{O}_7$ were provided by Aladdin Co., Ltd, China. All chemicals were used without further purification.

2.2. Synthesis of the NiO HoMS nanoreactors

The NiO HoMS nanoreactors were synthesized by direct calcination of coordination nanospheres of Ni^{2+} and tannic acid (Ni-TA), which were prepared according to a sol-gel method we reported before [35]. The Ni-TA polymer nanospheres were calcined in air at 400 °C and 600 °C for 2 h to synthesize 3-shelled and 2-shelled NiO HoMS, respectively. Bulky NiO nanoparticles was also prepared as a control by calcining Ni-TA polymer nanospheres at 700 °C for 1 h. The ramping rate was set as 2 °C/min.

2.3. Characterizations

Field-emission scanning electron microscope (SEM) was taken by a scanning electron microscope (Hitachi, S-4800). Transmission electron microscopy (TEM) was performed on a transmission electron microscope (Hitachi, JEM-F200). Energy-dispersive X-ray spectroscopy (EDS) was collected by an Oxford X-max 100TLE X-ray detector. XRD was taken by an X-Ray Diffractometer with Cu K α radiation (Bruker D8 ADVANCE). The scan was performed from 20 range from 20° to 90° with a scan rate of 2°/min. The step size was set as 0.02°. X-ray photoelectron spectroscopy (XPS) was performed on a Kratos AXIS Ultra DLD system (Thermo Fisher ESCALAB Xi⁺). The X-ray irradiation source was Al/Mg K α . The concentration of leached Ni^{2+} was determined by an inductively coupled plasma-optical emission spectrometry (NexION 350D). Thermogravimetric analysis (TG) was conducted by using a thermal gravimetric analyzer (TG-209-F3, NETZSCH). The ramping rate was set as 10 °C/min. *In-situ* Raman spectroscopy was performed on a laser Raman spectrometer (Horiba/HR Evolution). The excitation wavelength and irradiation power were 633 nm and 0.08 mW, respectively. The electrochemical measurement was conducted on an electrochemical workstation (CHI 660E, CH Instrument). The counter electrode and reference electrode were platinum wire and saturated Ag/AgCl electrode, respectively. The synthesized NiO was used as the working electrode. NaCl (0.5 mM) was used as the electrolyte.

2.4. Catalysis experiments

The degradation of BPA was carried out in a glass beaker (100 mL) at room temperature. Typically, 0.05 g of NiO was dispersed in 50 mL of BPA solution (10 mg/L). After stirring for 30 min, certain amount of PDS solution (0.1 M) was added to initiate the oxidation. During the reaction, 0.5 mL of sample was taken at 0, 5, 10, 20, 30, 40, 50 and 60 min and then quenched by methanol for analysis. The concentration of BPA was measured by high-performance liquid chromatography (HPLC, Agilent, 1220 Infinity LC) equipped with a C18 column (100 mm × 2.7 mm). Acetonitrile and water were used as the mobile phase. The volume ratio was set as 60/40. The concentration of total organic carbon (TOC) was analyzed via a TOC-L analyzer (TOC-V CPR, Shimadzu) to evaluate the mineralization degree of BPA. A UV-vis spectrophotometer (UV-2600, Shimadzu) was applied to determine the concentration of PDS. Reactive oxygen species were identified by an electron paramagnetic resonance (EPR) spectrometer (EMXmicro-6/1, Bruker). The degradation intermediates of BPA were determined by an ultraperformance liquid chromatography-Quadrupole-time of flight mass spectrometer (UPLC-Q-TOF, WATERS I-Class VION IMS QTof).

2.5. Computational calculations

The calculations were performed by using the Vienna Ab initio Simulation Package (VASP). The exchange-correlation effects were described according to the generalized gradient approximation (GGA) within the Perdew-Burke-Ernzerhof (PBE) methods. The detailed information was described in Text 1 in the Supporting Information (SI).

3. Results and discussion

3.1. Synthesis and characterizations of the NiO HoMS nanoreactors

The NiO HoMS nanoreactors were prepared by thermal decomposition of nickel-polyphenol coordination nanospheres (denoted as Ni-TA) (Fig. 1a). The shell number was regulated by changing the calcination temperature. The NiO HoMS was mainly formed via a heterogeneous contraction process [36–39]. During the calcination process, the surface of Ni-TA polymer nanospheres was oxidized first along with the formation of an exterior shell of NiO with low crystallinity (Fig. S1). The volume change from coordination polymer (Ni-TA) to NiO induced

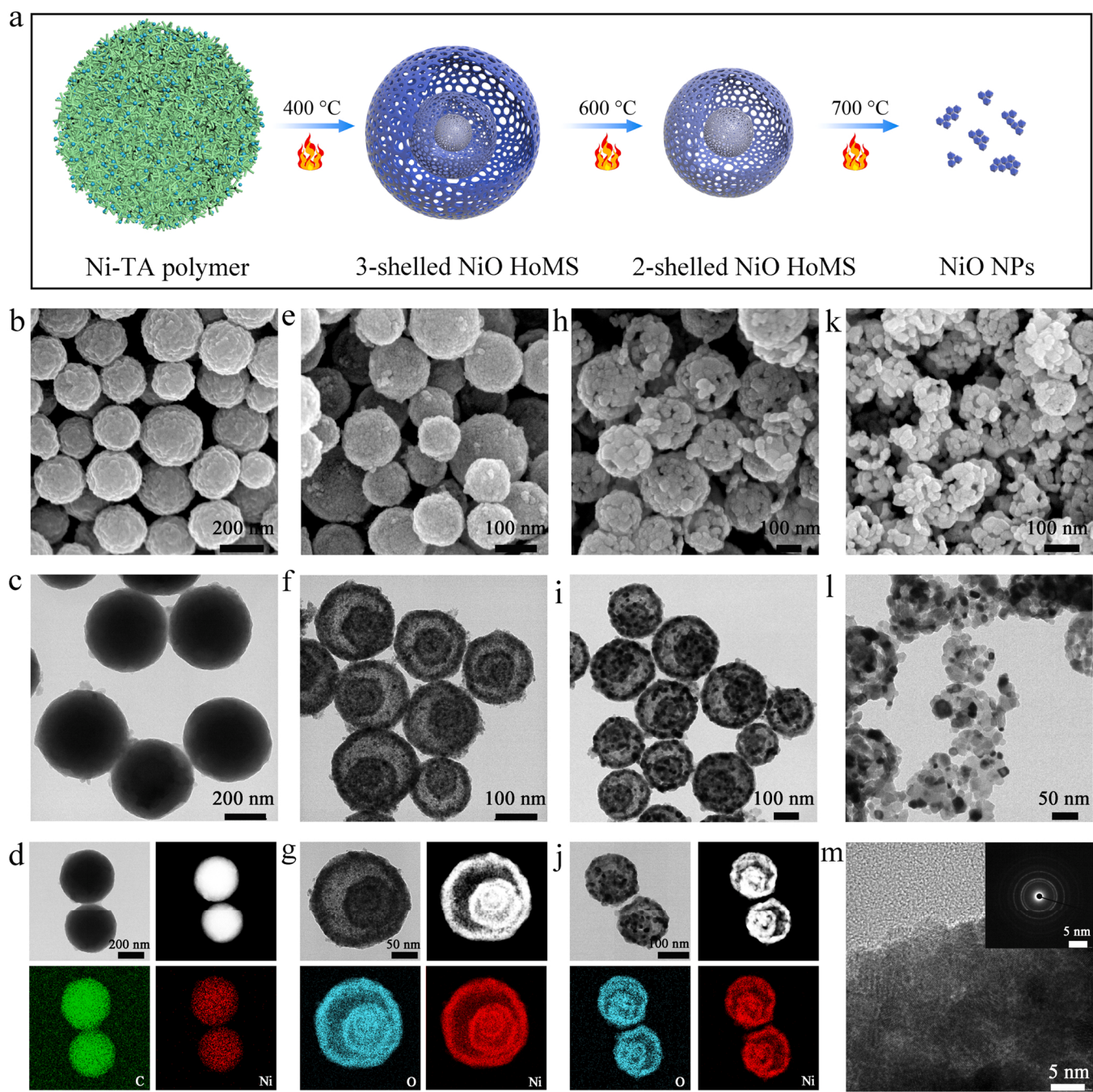


Fig. 1. (a) Schematic diagram for the formation of NiO HoMS with different shell numbers. SEM images, TEM images, high-magnified TEM images, STEM images and elemental mapping for (b-d) Ni-TA solid nanospheres, (e-g) 3-shelled NiO HoMS and (h-j) 2-shelled NiO HoMS. (k) SEM image and (l) TEM image for bulky NiO nanoparticles. (m) HR-TEM image and SAED pattern (inset) for the 3-shelled NiO HoMS.

residual stress in the oxide layer and caused spallation once the oxide layer reached a critical thickness, resulting in the formation of a yolk-shelled structure [40–43]. Upon prolonged calcination time, the same contraction process continued to take place for the inner Ni-TA polymer and a 3-shelled NiO HoMS was formed at 400 °C. By further increasing the temperature, the size of NiO crystals were continuously increased, and the innermost layer with low diameter fused with the middle layer [44], and then 2-shelled NiO HoMS was formed at 600 °C. When the calcination temperature was further increased to 700 °C, the hollow structure was collapsed due to the overgrowth of nanocrystals, resulting in the formation of bulky NiO nanoparticles (NPs).

SEM and TEM were applied to characterize the microstructure of Ni-TA nanospheres and the resultant NiO HoMS and bulky NiO

nano-particles. Ni-TA polymer showed spherical morphology and solid structure with Ni element homogeneously dispersed throughout the nanospheres (Fig. 2b-d). The 3-shelled NiO HoMS showed spherical morphology with hollow structure and multi shells (Figs. 2e, 2f). High-magnified TEM, STEM images and elemental mapping of Ni and O further confirmed the hollow structure with triple shells (Fig. 2g). High-resolution TEM (HR-TEM) image and selected area electron diffraction (SAED) pattern of the 3-shelled NiO HoMS revealed a crystallized structure (Fig. 2m). The 2-shelled NiO HoMS exhibited hollow structure with double shells as indicated by the SEM and TEM analysis (Fig. 2h-j). Large size of NiO crystals was observed compared with the 3-shelled NiO HoMS, resulting in porous structure like a nanocage. SEM and TEM images of the NiO nanoparticles showed aggregated structure (Figs. 2k,

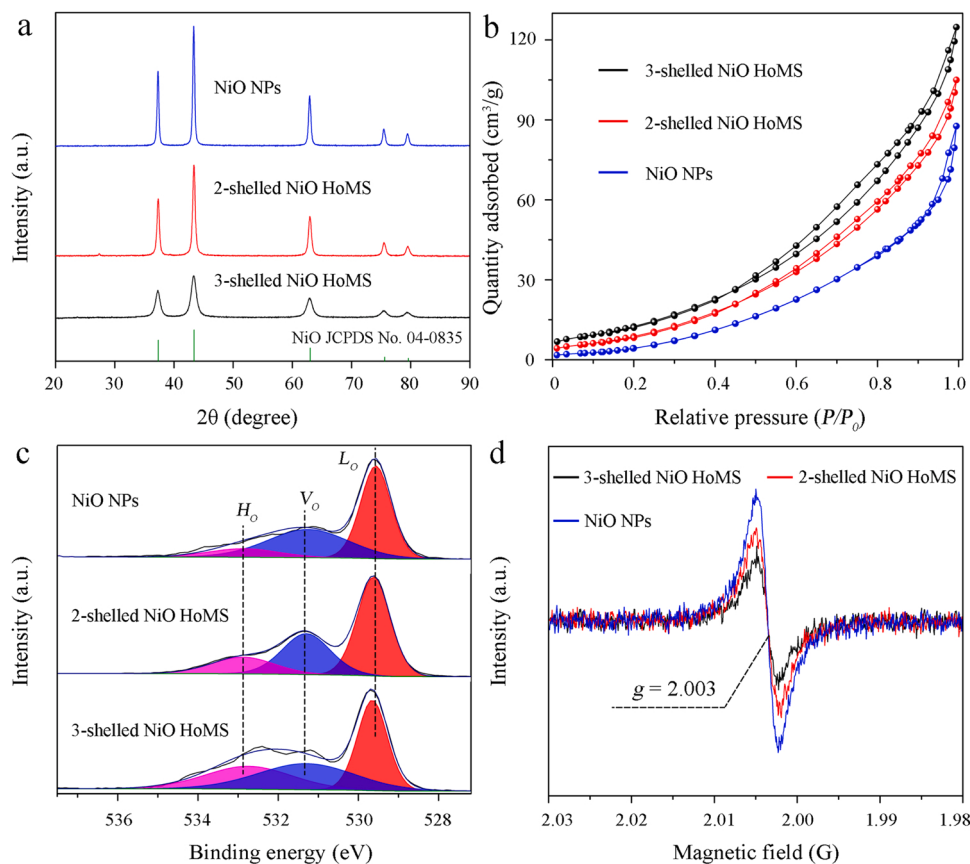


Fig. 2. (a) XRD profiles, (b) N_2 sorption isotherms, (c) O 1 s spectra and (d) solid EPR spectra for 3-shelled NiO HoMS, 2-shelled NiO HoMS and bulky NiO nanoparticles (NPs), respectively.

2I), which could be ascribed to the overgrowth of NiO crystals at a higher temperature.

The NiO HoMS and bulky NiO nanoparticles were characterized by different techniques. XRD profiles for 3-shelled NiO HoMS, 2-shelled NiO HoMS and bulky NiO nanoparticles displayed similar diffraction profiles that were well indexed to the cubic NiO (JCPDS No. 04-0835) (Fig. 2a) [45]. The increased peak intensity upon increasing the temperature suggested a larger size of NiO crystals at higher temperatures. N_2 sorption isotherms of the 3-shelled NiO HoMS, 2-shelled NiO HoMS and NiO nanoparticles exhibited similar hysteresis loops in the relative pressure ranging from 0.4 to 0.9, indicating the similar mesoporous structure (Fig. 2b). The BET surface area of 3-shelled NiO HoMS, 2-shelled NiO HoMS and NiO nanoparticles was determined to be 51.6, 35.5 and $22.7 \text{ m}^2/\text{g}$, respectively. The higher surface area of the NiO HoMS should be ascribed to the hollow multi-shelled structure [25,46]. Their pore sizes were centered at 6.0, 5.6 and 5.3 nm, respectively (Fig. S2). XPS spectra of Ni 2p for 3-shelled, 2-shelled NiO HoMS and NiO nanoparticles showed the similar profiles, revealing the same oxidation state of Ni species (Fig. S3). The O 1 s spectrum for the 3-shelled NiO HoMS displayed characteristic peaks of lattice oxygen (L_O), oxygen vacancy (V_O) and surface adsorbed H_2O (H_O) at 529.65 eV, 531.30 eV and 532.74 eV, respectively (Fig. 2c) [47,48]. Peaks of L_O , V_O and H_O were also observed in 2-shelled NiO HoMS and NiO nanoparticles with binding energies close to that of 3-shelled NiO HoMS (Table S1). The content of V_O in 3-shelled, 2-shelled NiO HoMS and NiO nanoparticles was determined to be 27.7%, 31.3% and 38.1%, respectively [17,30]. The increased V_O content upon increasing the temperature could be ascribed to the unique synthesis process of NiO, in which formation of NiO and combustion of poly TA occurred concurrently (Fig. 1a). The decomposition of poly TA took part of oxygen from NiO, resulting in the formation of V_O [30,32] (Fig. S4). Increasing the

temperature favored the total decomposition of poly TA and thus led to higher V_O content. EPR test at -196°C was also performed to verify the presence of surface V_O . Typical peaks at $g = 2.003$ were displayed for 3-shelled, 2-shelled NiO HoMS and bulky NiO nanoparticles (Fig. 2d), further confirming the formation of V_O [49]. The content of V_O increased upon increasing the temperature as indicated by the enhanced peak intensity, agreeing well with the XPS result. The above results revealed that the 3-shelled NiO HoMS, 2-shelled NiO HoMS and bulky NiO nanoparticles had similar physicochemical properties, which conferred the logical rationality to analyze the nanoconfinement effect of hollow multi-shelled structure through comparing their catalytic performances.

3.2. Catalytic performance and degradation pathway

Fig. 3a showed the degradation of BPA over NiO HoMS nanoreactors and NiO nanoparticles through PDS activation. PDS alone and homogeneous catalysis by leached Ni^{2+} (0.49 mg/L) induced negligible BPA removal efficiency (Fig. S5), indicating the degradation of BPA over the NiO HoMS nanoreactors mainly occurred via heterogeneous reactions [50]. The NiO HoMS nanoreactors were more effective toward BPA degradation than NiO nanoparticles. Complete BPA removal was obtained over 3-shelled NiO HoMS within 60 min, whereas NiO nanoparticles only degraded $\sim 40\%$ of BPA under the same reaction condition. The kinetic rate of BPA degradation over the 3-shelled NiO HoMS was calculated to be 0.08 min^{-1} according to the pseudo first-order kinetic model, which was 8 times higher than that over the NiO nanoparticles (Fig. 3b). The mineralization efficiency of BPA (79.2%) over the 3-shelled NiO HoMS was much higher than that over the NiO nanoparticles (29.8%) as well (Fig. 3c). Moreover, the 3-shelled NiO HoMS was also more effective toward BPA degradation compared with the 2-shelled NiO HoMS. The normalized kinetic rate constants

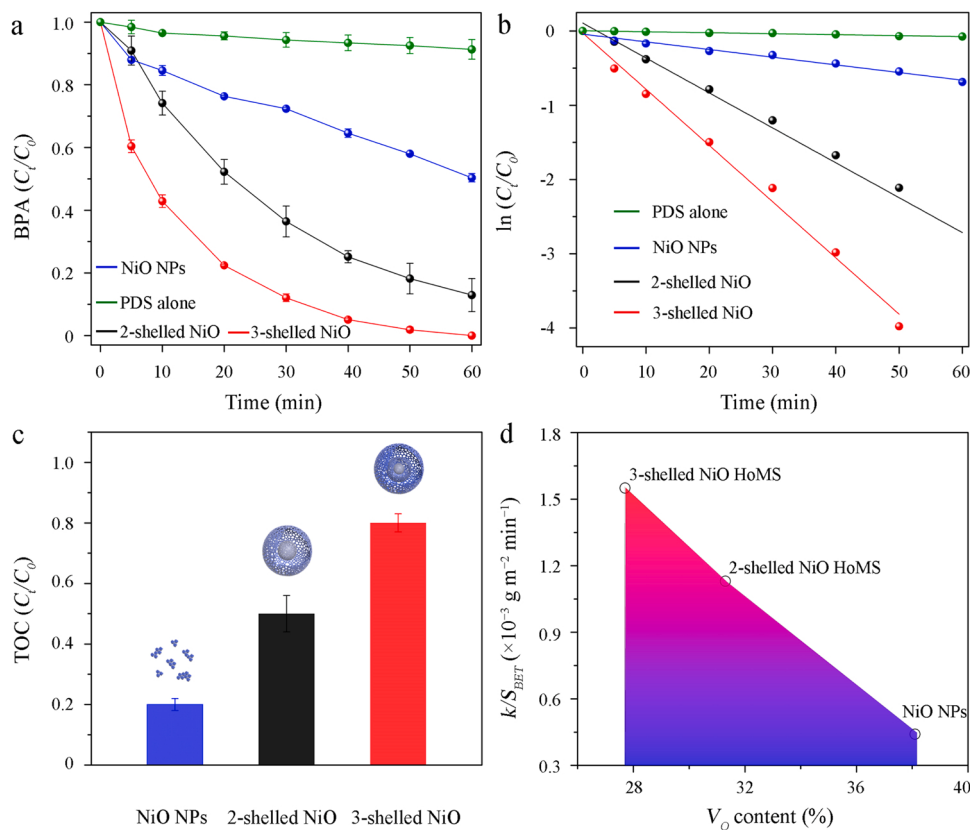


Fig. 3. (a) Degradation of BPA over 3-shelled and 2-shelled NiO HoMS and NiO nanoparticles (NPs) through PDS activation and corresponding (b) kinetic plots and (c) TOC removal efficiencies. (d) Normalized kinetic rates (k/S_{BET}) versus V_O contents for 3-shelled and 2-shelled NiO HoMS and NiO nanoparticles.

(k/S_{BET}) for 3-shelled and 2-shelled NiO HoMS nanoreactors and NiO nanoparticles were calculated to be 1.55×10^{-3} , 1.13×10^{-3} and $0.44 \times 10^{-3} \text{ g m}^{-2} \text{ min}^{-1}$ respectively, excluding the effect of surface area on the enhanced catalytic efficiency. These results indicated that the catalytic efficiency of the NiO HoMS nanoreactors was mainly depended on the hollow structure and number of shells. Interestingly, the degradation of BPA was not determined by the V_O content, which were recognized as the active sites for all the NiO catalysts (discussed in Section 3.3). NiO nanoparticles had the highest V_O content but exhibited the lowest kinetic rate and mineralization degree (Figs. 3c, 3d). This was distinctly different from previous researches, in which higher V_O content generally led to better catalytic performance [17,18]. The results indicated that the hollow multi-shelled structure mainly contributed to the enhanced catalytic efficiency of NiO HoMS nanoreactors in this work. It is probably because of the nanoconfinement effect induced by the hollow multi-shelled structure, which has been widely reported to be able to boost the catalytic efficiency of heterogeneous reactions [26,28].

The degradation pathway (radical vs. nonradical) of BPA over the NiO HoMS nanoreactors was investigated via EPR tests and chemical quenching experiments. The 3-shelled NiO HoMS was used in the experiments since it exhibited the best catalytic performance. As shown in Fig. 4a, no signal was detected when DMPO was used as a trapping agent, suggesting neither $\text{SO}_4^{\cdot-}$ nor HO^{\cdot} was produced during the activation of PDS [11]. Chemical quenching experiments using methanol (MeOH) as a scavenger revealed the degradation of BPA was only slightly inhibited even when excess amount (1000 mM) of MeOH was added, further revealing the absence of $\text{SO}_4^{\cdot-}$ and HO^{\cdot} (Fig. 4b). The signal of superoxide radical ($\text{O}_2^{\cdot-}$) was not detected either and quenching experiments by *p*-benzoquinone (BQ) showed BPA removal efficiency was not inhibited (Fig. S6). Besides, quenching experiments for surface-bonded reactive species by potassium iodide (KI) also revealed that BPA removal was not influenced (Fig. S7). These results revealed that

radicals were not produced and involved in the degradation of BPA [11, 12]. When TEMP was used as the spin trapping agent, however, signals of singlet oxygen (${}^1\text{O}_2$) were identified (Fig. 4c). As TEMP alone was ineffective to active PDS to produce ${}^1\text{O}_2$ (Fig. S8), it indicated that the generation of ${}^1\text{O}_2$ was ascribed to the activation of PDS over NiO HoMS nanoreactors. However, the intensity of the TEMP- ${}^1\text{O}_2$ adduct was not varied upon increasing the reaction time, suggesting ${}^1\text{O}_2$ may not participated into the degradation of BPA [33]. Furthermore, only a slight decrease of BPA removal was observed in the chemical quenching experiments using L-histidine as a scavenger (Fig. 4d). As a reductive agent, L-histidine is able to react with PDS molecules [4]. For example, 31% of PDS was decomposed by 0.1 M of L-histidine alone in 60 min (Fig. S9). That was to say, the inhibition of BPA removal caused by L-histidine was possibly due to the consumption of PDS by L-histidine rather than the quenching of ${}^1\text{O}_2$ [51]. Therefore, the degradation of BPA over the NiO HoMS nanoreactors was not dominated by reactive oxygen species like $\text{SO}_4^{\cdot-}$, HO^{\cdot} , $\text{O}_2^{\cdot-}$ and ${}^1\text{O}_2$.

Electron transfer regime has been also frequently reported for organics degradation in PDS-based oxidation processes [13–15]. Chemical quenching experiments for free electrons was carried out to explore the electron transfer mechanism. As shown in Fig. 4c and S10, the degradation of BPA was strongly inhibited when $\text{K}_2\text{Cr}_2\text{O}_7$ was introduced. $\text{K}_2\text{Cr}_2\text{O}_7$ has been widely used as a scavenger of electrons in photocatalysis and persulfate-based oxidation processes [13]. The significant inhibitory effect suggested that the degradation of BPA in the NiO HoMS + PDS system was dominated by the electron transfer mechanism. The enhanced decomposition of PDS by NiO HoMS in the presence of BPA further confirmed the electron transfer regime. As shown in Fig. S11, the decomposition efficiency of PDS by NiO HoMS increased from 32.4% to 43.6% when 5 mg/L of BPA was added. The decomposition of PDS was increased upon increasing the dosage of BPA, further revealing the degradation of BPA was associated with the electron transfer between

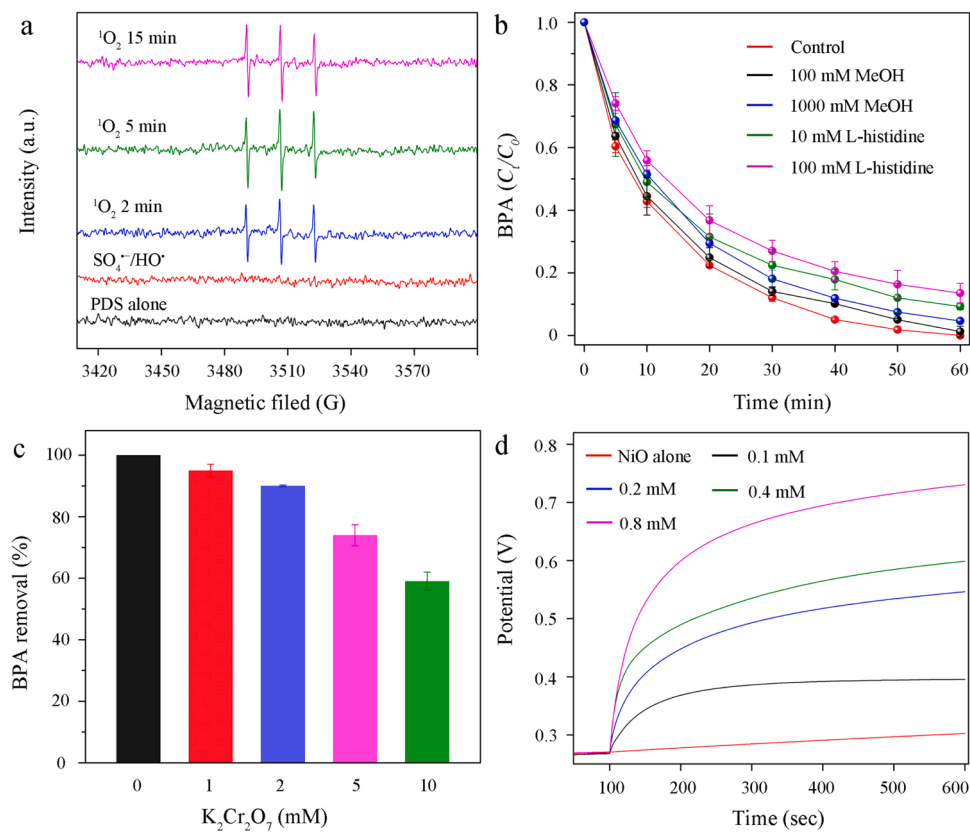


Fig. 4. (a) EPR tests for $\text{SO}_4^{2-}/\text{HO}^\bullet$ and $^1\text{O}_2$ using DMPO and TEMP as the spin trapping agent, respectively. (b) Quenching experiments for SO_4^{2-} and HO^\bullet and $^1\text{O}_2$ using MeOH and L-histidine as the scavenger, respectively. (c) Quenching experiments for electrons using $\text{K}_2\text{Cr}_2\text{O}_7$ as the scavenger. (d) OCP curves of 3-shelled NiO HoMS anode in the presence of PDS with different concentrations.

PDS and BPA molecules. *In-situ* electrochemical analysis was performed to further confirm the electron transfer mechanism. Open circuit potential (OCP) tests revealed that the potential was increased upon increasing the concentration of PDS (Fig. 4d), indicating the formation of PDS complex on the surface of NiO HoMS nanoreactors [34,52]. Chronoamperometry test revealed the current output increased significantly after the addition of PDS and BPA (Fig. S12), suggesting an electron transfer among the surface bonded-PDS complex and BPA molecules [34]. Linear sweep voltammetry (LSV) measurement revealed the addition of PDS increased the current output (Fig. S13). The current density was further increased after the addition of BPA and increased upon increasing the dosage, also validating an electron transfer from

BPA to the surface bonded-PDS complex [14,19]. Therefore, the above results revealed that the degradation of BPA in the NiO HoMS + PDS system followed a nonradical oxidation pathway based on electron transfer process.

3.3. Mechanism of PDS activation over the NiO HoMS nanoreactors

In metal oxides-initiated PDS activation, the redox cycle of metal species (M^{n+1}/M^{n+}) generally induced the activation of PDS [29,30]. To verify the mechanism of PDS activation over the 3-shelled NiO HoMS, the variation of chemical states of Ni species was investigated via XPS analysis. The XPS spectra of $\text{Ni } 2p_{3/2}$ for fresh NiO HoMS displayed two

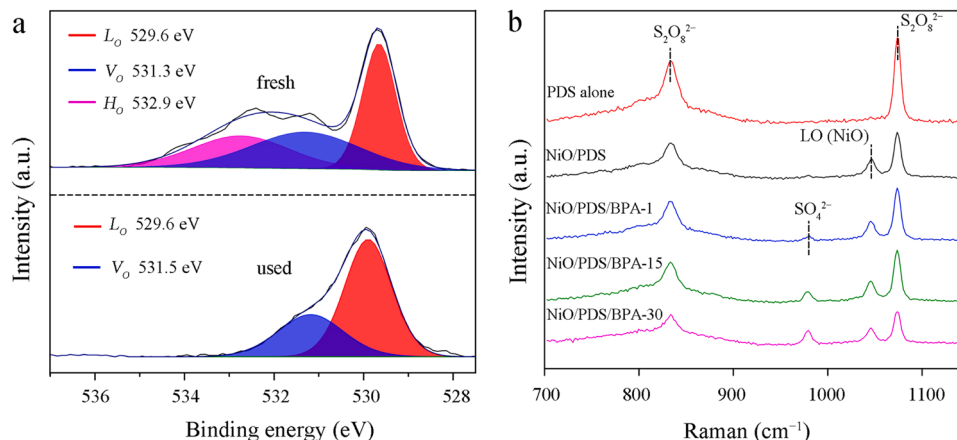


Fig. 5. (a) XPS spectra of O 1 s before and after the catalysis reaction. (b) *In-situ* Raman spectra of PDS alone, NiO/PDS and NiO/PDS/BPA at different reaction times. NiO/PDS/BPA- t stood for the reaction at time t ($t = 1, 15, 30$ min); LO stood for longitudinal optical phonon mode of NiO.

peaks at 853.6 eV and 855.2 eV, which were assigned to Ni^{2+} and Ni^{3+} , respectively (Fig. S14) [53,54]. After the catalysis reaction, no describable change of the valence states of Ni was observed. It indicated that activation of PDS over the NiO HoMS nanoreactors was not due to the redox cycle of $\text{Ni}^{2+}/\text{Ni}^{3+}$ [30]. However, significant change was observed in the XPS spectra of O 1 s after the catalysis reaction. As shown in Fig. 5a, surface-adsorbed oxygen (H_O) at 532.9 eV was vanished while the content of surface oxygen vacancy (V_O) at 531.3 eV was declined from 38.1% to 33.3% after the catalysis reaction [55]. It revealed that surface V_O was the possible active site of NiO HoMS toward PDS activation. *In-situ* Raman spectroscopy revealed that PDS molecules were firstly adsorbed on the surface of NiO HoMS nanoreactors via forming surface bonded-PDS complex (Fig. 5b, S15). When reacted with BPA, the surface bonded-PDS complex was gradually decomposed to SO_4^{2-} (981 cm⁻¹) by abstracting electrons from BPA molecules [56]. It led to continuous decomposition of PDS and degradation of BPA as indicated by the gradually decreased peak intensity of $\text{S}_2\text{O}_8^{2-}$ (835 and 1075 cm⁻¹) with the reaction time (Fig. 5b) [56,57].

V_O being the active site of PDS activation was further evaluated through DFT calculations. NiO (111) facets with and without V_O were employed as models for the DFT investigations (Figs. 6a, 6b, S16) [17, 58]. The charge distributions of Ni atoms of the NiO (111) showed that the V_O -connected Ni atoms possessed lower positive charge as compared to the intact NiO (111) surface (Figs. 6c, 6d), suggesting the electron accumulation and redistribution mediated by V_O [17,18]. The calculations of PDS adsorption on NiO (111) with and without V_O revealed that the adsorption energy of PDS molecules was increased from -0.46 eV to -3.62 eV after the introduction of V_O (Figs. 6e, 6f). The surface V_O enormously facilitated the chemical adsorption of PDS, and then favored the formation of NiO-PDS complex on V_O -rich surface. Besides, the length of O-O bond of PDS molecule was elongated from 1.27 Å to 1.50 Å when V_O was introduced, also demonstrating PDS adsorbed on V_O -rich NiO was more easily activated [59]. Altogether, the DFT calculation results elaborated the crucial role of V_O in terms of electron accumulation and adsorption enhancement of PDS, which induced activation of PDS over the NiO HoMS nanoreactors.

3.4. Insights into the enhanced catalytic efficiency of the NiO HoMS nanoreactors

In heterogeneous catalysis reactions, the catalytic efficiency of nanomaterials is generally depended on the number of active sites [29]. As V_O acted as the active site of PDS activation, the enhanced catalytic performance of the NiO HoMS nanoreactors theoretically should be

ascribed to the higher V_O content. However, the kinetic rates and mineralization efficiencies of BPA over the synthesized NiO were inversely proportional to the V_O contents (Fig. 3d). The 3-shelled NiO HoMS had the lowest V_O content but exhibited the highest catalytic performance. It indicated that the enhanced catalytic efficiency of NiO HoMS nanoreactors was not due to the surface V_O . Nanomaterials with hollow multi-shelled structure can provide a unique nanospace for locally confining reactants and increasing their instantaneous concentrations [28,60]. The HoMS induced nanoconfinement effect could greatly improve the catalytic efficiency of heterogeneous reactions [61]. Herein, the catalytic performance of the NiO HoMS nanoreactors was highly depended on the hollow structure and greatly influenced by the number of shells (Fig. 3). Compared with bulky NiO nanoparticles, the NiO HoMS was more effective toward BPA degradation. Moreover, the kinetic rate and mineralization efficiency was further enhanced when the shell number was increased from 2 to 3. The results revealed that the nanoconfinement induced by the hollow multi-shelled structure mainly contributed to the enhanced catalytic efficiency of NiO HoMS nanoreactors.

To verify the nanoconfinement effect, finite element analysis was conducted by simulating the concentration gradient distribution of BPA and its degradation intermediates (shown in Fig. S17, Table S2) over NiO HoMS nanoreactors and bulky NiO nanoparticles [60,62]. Three models of NiO nanoparticle, 2-shelled and 3-shelled NiO HoMS nanosphere were established to simulate the concentration gradient distribution over these individual particles. Based on the mechanism of PDS activation, we posited that PDS was firstly activated via forming surface-bonded PDS complex on the surface of NiO HoMS. After that, BPA molecules diffused into the multi-shelled nanoreactor, underwent reaction with PDS complex and evolved into intermediates, which then desorbed from NiO surface for further oxidation (Fig. 7a). As shown in Fig. 7b-d, the concentration gradient distribution over the NiO nanoparticle was much lower than that over 2-shelled and 3-shelled NiO HoMS. It indicated that more BPA/intermediates were confined and accumulated in the void spaces of 2-shelled and 3-shelled models compared to the nanoparticle model, clarifying the nanoconfinement effect of NiO HoMS nanoreactors. This could be ascribed to the temporal-spatial ordering behaviour of the hollow multi-shelled structure [23,24,28]. Degradation of BPA over the 3-shelled NiO HoMS would go through the outermost shell, middle shell and innermost shell in sequence (Fig. 7a). The multi-shells increased the collision probability between BPA and surface-bonded PDS complex and thus increased the instantaneous concentration of BPA/intermediates in the void spaces. For reactions over the bulky NiO nanoparticles, however, BPA molecules

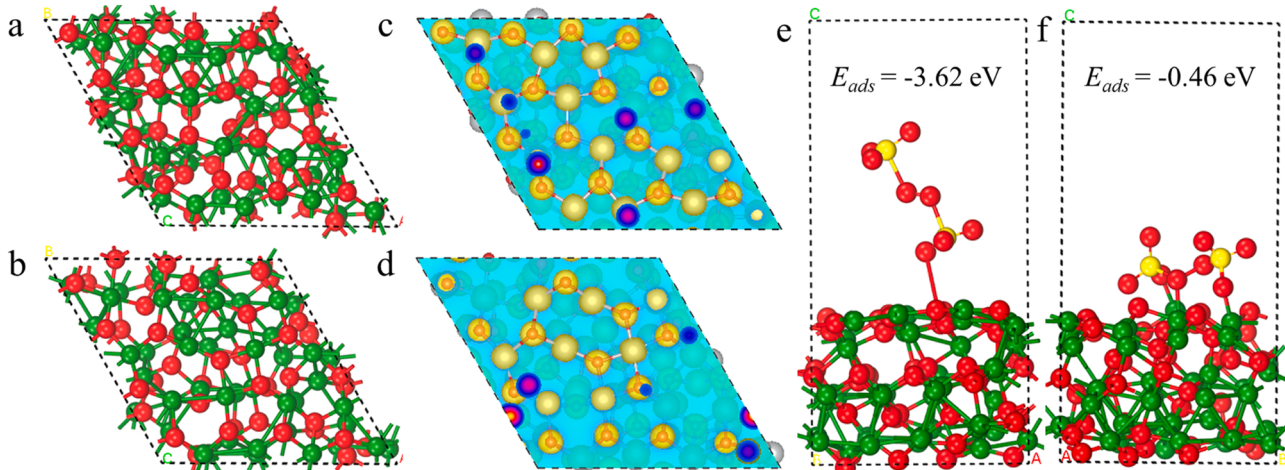


Fig. 6. Top view of the optimized configurations of NiO (111) with (a) and without (b) oxygen vacancy. Charge distribution on the surface of the NiO (111) facets with (c) and without (d) oxygen vacancy after the configurations were optimized. Side view of the optimized configurations of PDS adsorption on NiO (111) with (e) and without (f) oxygen vacancy.

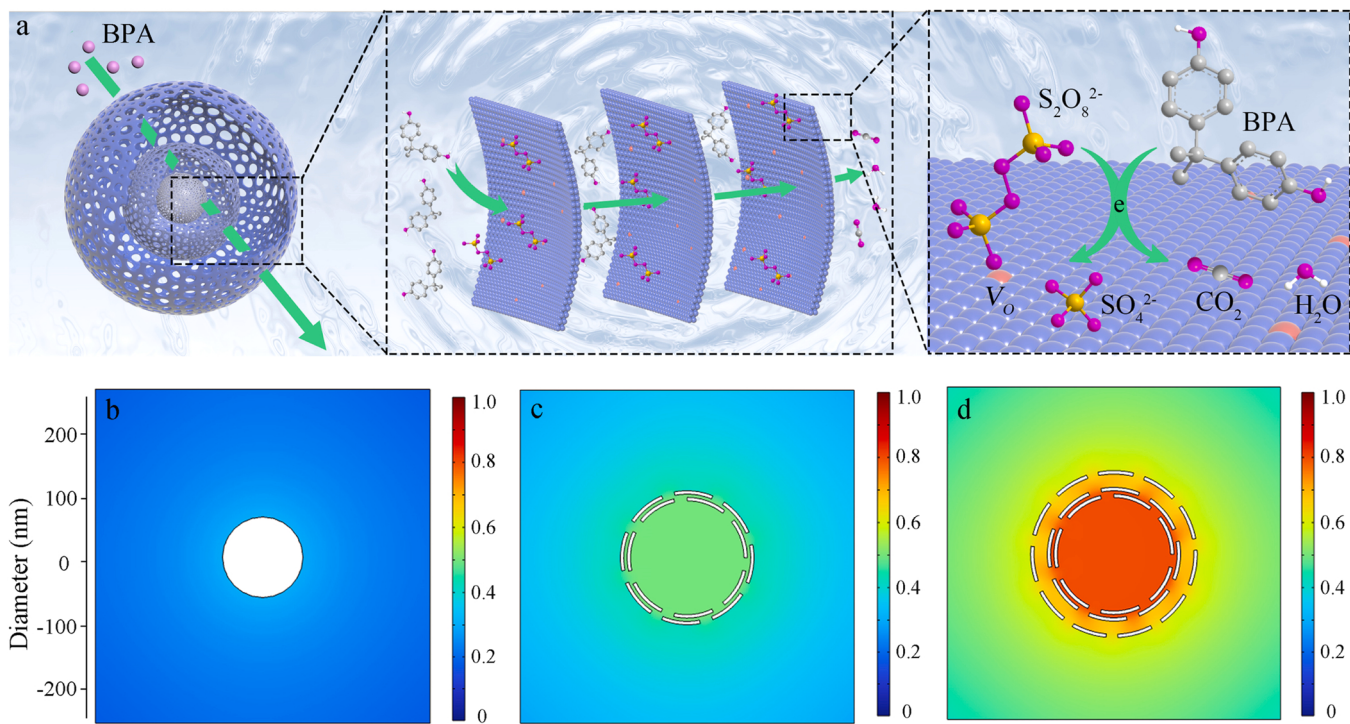


Fig. 7. (a) Schema for nanoconfined catalytic degradation of BPA over the NiO HoMS nanoreactors through electron transfer mechanism. The FEM simulated concentration gradient distribution of BPA and its degradation intermediates over (b) NiO nanoparticle, (c) 2-shelled and (d) 3-shelled NiO HoMS nanospheres, respectively.

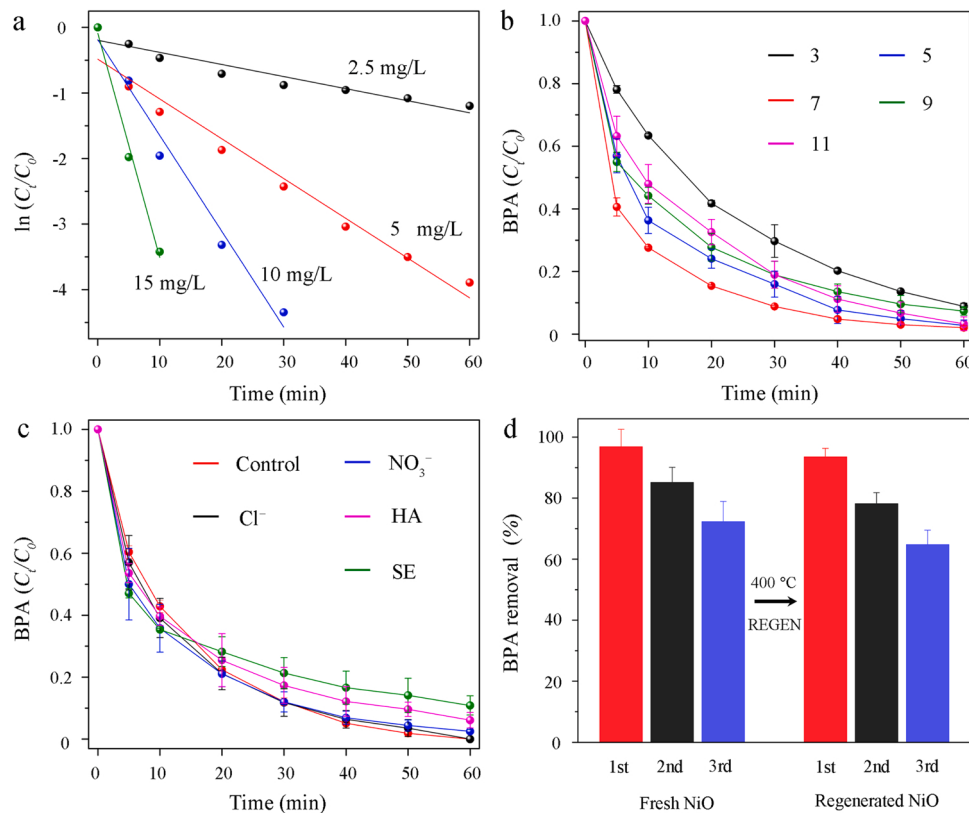


Fig. 8. Influence of (a) the dosage of 3-shelled NiO HoMS, (b) initial pH on the degradation of BPA. (c) Degradation of BPA in the presence of Cl^- (50 mM), NO_3^- (50 mM) and humic acid (HA, 50 mg/L) and in real secondary effluent (SE) of wastewater treatment plant. (d) Stability and regeneration of the 3-shelled NiO HoMS nanoreactors in consecutive runs. REGEN stood for regeneration via calcination at 400 °C.

unlikely experienced the sequent reactions but tended to escape from the catalyst surface. Therefore, FEM simulations combined with kinetic studies clarified that the nanoconfinement induced by the hollow multi-shelled structure was the dominant factor to improve the catalytic efficiency of the NiO HoMS nanoreactors.

3.5. Potential application of the NiO HoMS nanoreactors

As a typical nonradical oxidation, the electron transfer regime has shown great advantages in organics removal in terms of good resistance to background constituents and high utilization efficiency of PDS [12, 15]. Herein, the degradation efficiency of BPA over 3-shelled NiO HoMS under different experimental conditions was investigated to manifest the advantages. The NiO HoMS nanoreactors showed a superior catalytic performance at an extremely low concentration of PDS (0.1 mM) (Fig. S18a). Increasing the dosage of the NiO HoMS nanoreactors significantly enhanced BPA removal (Fig. S18b). When the dosage of the 3-shelled NiO HoMS was increased from 0.05 to 0.3 g/L, for example, the degradation kinetic rate was increased from 0.03 to 0.35 min⁻¹ (Fig. 8a). This was reasonable as more PDS would be activated when the dosage of NiO HoMS nanoreactors was increased. The results revealed that the NiO HoMS had a high utilization efficiency of PDS, and formation of surface-bonded PDS complex might be the rate-limiting step for BPA removal [34,63]. The degradation of BPA over the NiO HoMS nanoreactors was effective in a wide pH range (Fig. 8b, Fig. S19a). The removal efficiency of BPA maintained high from pH 3–11. In a heterogeneous reaction, the catalytic activity of metal oxides is generally sensitive to the variation of pH as it usually determines the electrostatic interactions between metal oxides and pollutants [64]. Herein, the pH_{pzc} of NiO HoMS nanoreactors was measured to be ~5.0 (Fig. S19b). The pKa value of BPA was reported to be 9.6/10.2 [65], and thus adsorption of BPA on NiO HoMS was negligible. On the other hand, it has been reported that the activity of metal catalysts was sensitive to changes in pH because surface hydroxyl groups tended to form on the surface of metal sites (M-OH) [45]. The insignificant pH effect on BPA removal indicated that Ni species did not participate into the reducible activation of PDS, but followed a nonradical pathway (e.g., electron transfer regime).

The influence of ubiquitous inorganic ions on BPA degradation was also investigated. Cl⁻ and NO₃⁻ hardly retarded the degradation of BPA even when the concentration was increased to 50 mM (Fig. S20, Fig. 8c). Natural organic matter (such as humic acid, HA) also exhibited limited influence on BPA removal in the concentration range from 5 to 50 mg/L (Fig. S21a, Fig. 8c). The slight decrease should be ascribed to the adsorption of HA on NiO HoMS nanoreactors and resultant coverage of catalytic sites [9]. The results further indicated that the degradation of BPA was not relied on radicals which were sensitive to inorganic ions and natural organic matters [66–68]. The good resistance to complex surroundings enabled outstanding performance in real water matrix. The removal of BPA in the secondary effluent (SE) of waste water treatment plant, surface water and groundwater were all > 90%, closing to that in ultrapure water (Fig. 8c, Fig. S21b).

The stability and reusability of the NiO HoMS nanoreactors was evaluated via consecutive degradation experiments. For the fresh 3-shelled NiO HoMS nanoreactors, BPA removal was still as high as 70% after three consecutive runs, revealing a good stability (Fig. 8d). The declined performance should be ascribed to the coverage of active sites by the degradation intermediates [3]. Moreover, the activity of the NiO HoMS nanoreactors could be effectively recovered via a facile calcination at 400 °C. The regenerated NiO HoMS could also degrade BPA effectively in consecutive runs with performance comparable with the fresh nanoreactors. The NiO HoMS nanoreactors were synthesized by using natural abundant plant polyphenol (e.g., TA) as a precursor and showed comparable catalytic performance with the reported NiO catalysts (Table S3). These unique properties combined with the outstanding performance in complicated experimental conditions made the NiO

HoMS nanoreactors a promising catalyst for wastewater decontamination.

4. Conclusion

In summary, for the first time, a series of NiO with different inner structures was designed as a nanoreactor of PDS activation to demonstrate the crucial role of the hollow multi-shelled structure for enhancing the catalytic efficiency of nonradical oxidation. The unique hollow multi-shelled structure induced void-confinement effect that increased the instantaneous concentration of reactants and thus led to enhanced decomposition of organic pollutants in electron transfer process based-nonradical oxidation. Surface oxygen vacancy mediated the electron transfer regime but did not dominate the catalytic efficiency. Kinetic studies and FEM simulation revealed the hollow multi-shelled structure, which increased the accessibility of active sites and enriched local concentration of reactants, mainly contributed to the enhanced catalytic efficiency of NiO HoMS nanoreactors. This work provided a guidance for designing highly efficient HoMS nanoreactors for improving the oxidation capacity of nonradical oxidation processes.

CRediT authorship contribution statement

Gen Wang: Formal analysis, Writing – original draft preparation, Conceptualization, Funding acquisition. **Ke Wang:** Investigation, Visualization. **Zhuoyue Liu:** Investigation, Visualization. **Youyou Feng:** Investigation, Visualization. **Shengjiang Yang:** Writing – review & editing. **Yaqiong Su:** Writing – review & editing. **Xufang Qian:** Writing – review & editing. **Pengkang Jin:** Writing – review & editing. **Jing Wei:** Writing – review & editing, Funding acquisition.

Declaration of Competing Interest

The authors declare that they have no known competing financial interests or personal relationships that could have appeared to influence the work reported in this paper.

Data Availability

Data will be made available on request.

Acknowledgments

This work was financially supported by the Postdoctoral Research Foundation of China (2020M673356), Natural Science Foundation of Shaanxi Province (Grant No. 2021JQ-503), Key Research and Development Program of Shaanxi (Program No. 2021GY-225), National Natural Science Foundation of China (Grant No. 21701130). The authors also thank eceshi (www.eceshi.com) for the kind assistance with ICP analysis. Supercomputing facilities were provided by Hefei Advanced Computing Center.

Appendix A. Supporting information

Supplementary data associated with this article can be found in the online version at [doi:10.1016/j.apcatb.2023.122359](https://doi.org/10.1016/j.apcatb.2023.122359).

References

- [1] Y. Yang, X. Zhang, J. Jiang, J. Han, W. Li, X. Li, K.M.Y. Leung, S.A. Snyder, P.J. Alvarez, Which micropollutants in water environments deserve more attention globally? *Environ. Sci. Technol.* 56 (1) (2022) 13–29.
- [2] S. Wang, J. Tian, Q. Wang, F. Xia, S. Gao, W. Shi, F. Cui, Development of CuO coated ceramic hollow fiber membrane for peroxymonosulfate activation: a highly efficient singlet oxygen-dominated oxidation process for bisphenol a degradation, *Appl. Catal. B* 256 (2019), 117783.

[3] G. Wang, W. An, Y. Zhang, Z. Liu, S. Yang, P. Jin, D. Ding, Mesoporous carbon framework supported Cu-Fe oxides as efficient peroxymonosulfate catalyst for sustained water remediation, *Chem. Eng. J.* 430 (2022), 133060.

[4] S. Zhu, X. Li, J. Kang, X. Duan, S. Wang, Persulfate activation on crystallographic manganese oxides: Mechanism of singlet oxygen evolution for nonradical selective degradation of aqueous contaminants, *Environ. Sci. Technol.* 53 (1) (2019) 307–315.

[5] Y. Liu, J. Luo, L. Tang, C. Feng, J. Wang, Y. Deng, H. Liu, J. Yu, H. Feng, J. Wang, Origin of the enhanced reusability and electron transfer of the carbon-coated Mn_3O_4 nanocube for persulfate activation, *ACS Catal.* 10 (24) (2020) 14857–14870.

[6] J. Chen, X. Zhou, P. Sun, Y. Zhang, C.H. Huang, Complexation enhances Cu(II)-activated peroxydisulfate: A novel activation mechanism and Cu(III) contribution, *Environ. Sci. Technol.* 53 (20) (2019) 11774–11782.

[7] Y. Wu, X. Chen, Y. Han, D. Yue, X. Cao, Y. Zhao, X. Qian, Highly efficient utilization of nano-Fe(0) embedded in mesoporous carbon for activation of peroxydisulfate, *Environ. Sci. Technol.* 53 (15) (2019) 9081–9090.

[8] J. Lee, U. von Gunten, J.H. Kim, Persulfate-based advanced oxidation: Critical assessment of opportunities and roadblocks, *Environ. Sci. Technol.* 54 (6) (2020) 3064–3081.

[9] G. Wang, Y. Zhang, L. Ge, Z. Liu, X. Zhu, S. Yang, P. Jin, X. Zeng, X. Zhang, Monodispersed CuO nanoparticles supported on mineral substrates for groundwater remediation via a nonradical pathway, *J. Hazard. Mater.* 429 (2022), 128282.

[10] Z. Yang, J. Qian, C. Shan, H. Li, Y. Yin, B. Pan, Toward selective oxidation of contaminants in aqueous systems, *Environ. Sci. Technol.* 55 (21) (2021) 14494–14514.

[11] W. Ren, L. Xiong, X. Yuan, Z. Yu, H. Zhang, X. Duan, S. Wang, Activation of peroxydisulfate on carbon nanotubes: electron-transfer mechanism, *Environ. Sci. Technol.* 53 (24) (2019) 14595–14603.

[12] X. Duan, H. Sun, Z. Shao, S. Wang, Nonradical reactions in environmental remediation processes: Uncertainty and challenges, *Appl. Catal. B* 224 (2018) 973–982.

[13] J. Yu, L. Tang, Y. Pang, G. Zeng, H. Feng, J. Zou, J. Wang, C. Feng, X. Zhu, X. Ouyang, J. Tan, Hierarchical porous biochar from shrimp shell for persulfate activation: a two-electron transfer path and key impact factors, *Appl. Catal. B* 260 (2020), 118160.

[14] H. Wang, W. Guo, B. Liu, Q. Wu, H. Luo, Q. Zhao, Q. Si, F. Sseguya, N. Ren, Edge-nitrogenated biochar for efficient peroxydisulfate activation: an electron transfer mechanism, *Water Res.* 160 (2019) 405–414.

[15] W. Ren, L. Xiong, G. Nie, H. Zhang, X. Duan, S. Wang, Insights into the electron-transfer regime of peroxydisulfate activation on carbon nanotubes: The role of oxygen functional groups, *Environ. Sci. Technol.* 54 (2) (2020) 1267–1275.

[16] X. Duan, H. Sun, S. Wang, Metal-free carbocatalysis in advanced oxidation reactions, *Acc. Chem. Res.* 51 (3) (2018) 678–687.

[17] L. Liu, Q. Liu, Y. Wang, J. Huang, W. Wang, L. Duan, X. Yang, X. Yu, X. Han, N. Liu, Nonradical activation of peroxydisulfate promoted by oxygen vacancy-laden NiO for catalytic phenol oxidative polymerization, *Appl. Catal. B* 254 (2019) 166–173.

[18] L. Liu, Y. Wang, Q. Liu, W. Wang, L. Duan, X. Yang, S. Yi, X. Xue, J. Zhang, Activating peroxydisulfate by morphology-dependent NiO catalysts: structural origin of different catalytic properties, *Appl. Catal. B* 256 (2019), 117806.

[19] W.D. Oh, Z. Dong, T.T. Lim, Generation of sulfate radical through heterogeneous catalysis for organic contaminants removal: Current development, challenges and prospects, *Appl. Catal. B* 194 (2016) 169–201.

[20] S. Yang, S. Xu, J. Tong, D. Ding, G. Wang, R. Chen, P. Jin, X. Wang, Overlooked role of nitrogen dopant in carbon catalysts for peroxymonosulfate activation: Intrinsic defects or extrinsic defects? *Appl. Catal. B* 295 (2021), 120291.

[21] G. Wang, S. Yang, L. Cao, P. Jin, X. Zeng, X. Zhang, J. Wei, Engineering mesoporous semiconducting metal oxides from metal-organic frameworks for gas sensing, *Coord. Chem. Rev.* 445 (2021), 214086.

[22] W. Zhu, Z. Chen, Y. Pan, R. Dai, Y. Wu, Z. Zhuang, D. Wang, Q. Peng, C. Chen, Y. Li, Functionalization of hollow nanomaterials for catalytic applications: nanoreactor construction, *Adv. Mater.* 31 (38) (2019) 1800426.

[23] N.L. Yang, Q. Li, D. Wang, J.Y. Wang, J.W. Wan, Hollow multishell structures exercise temporal-spatial ordering and dynamic smart behaviour, *Nat. Rev. Chem.* 4 (2020) 159–168.

[24] L. Wang, J.W. Wan, J.Y. Wang, D. Wang, Small structures bring big things: performance control of hollow multishelled structures, *Small Struct.* 2 (2021) 2000041.

[25] L. Wang, J. Wei, J.Y. Wang, D. Wang, Hollow multishelled structures for promising applications: understanding the structure-performance correlation, *Acc. Chem. Res.* 52 (2019) 2169–2178.

[26] W. Li, X. He, B. Li, B. Zhang, T. Liu, Y. Hu, J. Ma, Structural tuning of multishelled hollow microspheres for boosted peroxymonosulfate activation and selectivity: role of surface superoxide radical, *Appl. Catal. B* 305 (2022), 121019.

[27] M. Zhang, C. Xiao, X. Yan, S. Chen, C. Wang, R. Luo, J. Qi, X. Sun, L. Wang, J. Li, Efficient removal of organic pollutants by metal-organic framework derived Co/C yolk-shell nanoreactors: size-exclusion and confinement effect, *Environ. Sci. Technol.* 54 (16) (2020) 10289–10300.

[28] C. Dong, Q. Yu, R.P. Ye, P.P. Su, J. Liu, G.H. Wang, Hollow carbon sphere nanoreactors loaded with PdCu nanoparticles: Void-confinement effects in liquid-phase hydrogenations, *Angew. Chem. Int. Ed.* 59 (2020) 18374–18379.

[29] M. Wang, Y. Cui, H. Cao, P. Wei, C. Chen, X. Li, J. Xu, G. Sheng, Activating peroxydisulfate with $Co_3O_4/NiCo_2O_4$ double-shelled nanocages to selectively degrade bisphenol A-A nonradical oxidation process, *Appl. Catal. B* 282 (2021), 119585.

[30] J. Hu, X. Zeng, G. Wang, B. Qian, Y. Liu, X. Hu, B. He, L. Zhang, X. Zhang, Modulating mesoporous Co_3O_4 hollow nanospheres with oxygen vacancies for highly efficient peroxymonosulfate activation, *Chem. Eng. J.* 400 (2020), 125869.

[31] Y. Bu, H. Li, W. Yu, Y. Pan, L. Li, Y. Wang, L. Pu, J. Ding, G. Gao, B. Pan, Peroxydisulfate activation and singlet oxygen generation by oxygen vacancy for degradation of contaminants, *Environ. Sci. Technol.* 55 (3) (2021) 2110–2120.

[32] J. Hu, B. Qian, X. Zeng, Y. Qi, Y. Liu, L. Zhang, X. Zhang, Oxygen vacant Co_3O_4 in situ embedded on carbon spheres: cooperatively tuning electron transfer for boosted peroxymonosulfate activation, *J. Mater. Chem. A* 9 (2021) 16489.

[33] H. Zhang, C. Li, L. Lyu, C. Hu, Surface oxygen vacancy inducing peroxymonosulfate activation through electron donation of pollutants over cobalt-zinc ferrite for water purification, *Appl. Catal. B* 270 (2020), 118874.

[34] G. Wang, L. Ge, Z. Liu, X. Zhu, S. Yang, K. Wu, P. Jin, X. Zeng, X. Zhang, Activation of peroxydisulfate by defect-rich CuO nanoparticles supported on layered MgO for organic pollutants degradation: An electron transfer mechanism, *Chem. Eng. J.* 431 (2021), 134026.

[35] J. Wei, G. Wang, F. Chen, M. Bai, Y. Liang, H. Wang, D. Zhao, Y. Zhao, Sol-gel synthesis of metal-phenolic coordination spheres and their derived carbon composites, *Angew. Chem. Int. Ed.* 57 (31) (2018) 9838–9843.

[36] G. Wang, X. Zhou, J. Qin, Y. Liang, B. Feng, Y. Deng, Y. Zhao, J. Wei, General synthesis of mixed semiconducting metal oxide hollow spheres with tunable compositions for low-temperature chemiresistive sensing, *ACS Appl. Mater. Interface* 11 (38) (2019) 35060–35067.

[37] J.Y. Wang, Z.M. Wang, D. Mao, D. Wang, The development of hollow multishelled structure: from the innovation of synthetic method to the discovery of new characteristics, *Sci. China Chem.* 65 (2022) 7–19.

[38] D. Wang, B. Wang, X.X. Zhao, D.W. Li, R.B. Yu, Formation of multi-shelled nickel-based sulfides hollow spheres for rechargeable alkaline batteries, *Inorg. Chem. Front.* 5 (2018) 535–540.

[39] D. Mao, J.W. Wan, J.Y. Wang, D. Wang, Sequential templating approach: a groundbreaking strategy to create hollow multishelled structures, *Adv. Mater.* 31 (2019) 1802874.

[40] G. Wang, J. Qin, Y. Feng, B. Feng, S. Yang, Z. Wang, Y. Zhao, J. Wei, Sol-gel synthesis of spherical mesoporous high-entropy oxides, *ACS Appl. Mater. Interface* 12 (40) (2020) 45155–45164.

[41] Y. Feng, P. Li, J. Wei, Engineering functional mesoporous materials from plant polyphenol-based coordination polymers, *Coord. Chem. Rev.* 468 (2022), 21469.

[42] X.Y. Lai, J. Li, B.A. Korgel, Z.H. Dong, Z.M. Li, F.B. Su, J. Du, D. Wang, General synthesis and gas-sensing properties of multiple-shell metal oxide hollow microspheres, *Angew. Chem. Int. Ed.* 50 (2011) 2738–2741.

[43] H. Li, H.R. Ma, M. Yang, B. Wang, H. Shao, L. Wang, R.B. Yu, D. Wang, Highly controlled synthesis of multi-shelled NiO hollow microspheres for enhanced lithium storage properties, *Mater. Res. Bull.* 87 (2017) 224–229.

[44] G. Zhan, H. Zeng, A synthetic protocol for preparation of binary multi-shelled hollow spheres and their enhanced oxidation application, *Chem. Mater.* 29 (23) (2017) 10104–10112.

[45] D. Yue, C. Guo, X. Yan, R. Wang, M. Fang, Y. Wu, X. Qian, Y. Zhao, Secondary battery inspired NiO nanosheets with rich Ni(III) defects for enhancing persulfates activation in phenol waste water degradation, *Chem. Eng. J.* 360 (2019) 97–103.

[46] L. Lai, J.E. Halpert, D. Wang, Recent advances in micro-/nano-structured hollow spheres for energy applications: from simple to complex systems, *Energy Environ. Sci.* 5 (2012) 5604–5618.

[47] X. Chen, T. Zhang, M. Kan, D. Song, J. Jia, Y. Zhao, X. Qian, Binderless and oxygen vacancies rich FeNi/graphitized mesoporous carbon/Ni foam for electrocatalytic reduction of nitrate, *Environ. Sci. Technol.* 54 (20) (2020) 13344–13353.

[48] L. Wu, Z. Sun, Y. Zhen, S. Zhu, C. Yang, J. Lu, Y. Tian, D. Zhong, J. Ma, Oxygen vacancy-induced nonradical degradation of organics: Critical trigger of oxygen (O_2) in the Fe-Co LDH/peroxymonosulfate system, *Environ. Sci. Technol.* 55 (22) (2021) 15400–15411.

[49] S. Zhan, H. Zhang, X. Mi, Y. Zhao, C. Hu, L. Lyu, Efficient Fenton-like process for pollutant removal in electron-rich/poor reaction sites induced by surface oxygen vacancy over cobalt-zinc oxides, *Environ. Sci. Technol.* 54 (13) (2020) 8333–8343.

[50] G. Liu, T. Zhang, T. Wang, H. Yamashita, Y. Zhao, X. Qian, Peroxydisulfate activation by photo-generated charges on mesoporous carbon nitride for removal of chlorophenols, *Appl. Catal. B* 296 (2021), 120370.

[51] N. Li, R. Li, X. Duan, B. Yan, W. Liu, Z. Cheng, G. Chen, L. Hou, S. Wang, Correlation of active sites to generated reactive species and degradation routes of organics in peroxymonosulfate activation by Co-loaded carbon, *Environ. Sci. Technol.* 55 (23) (2021) 16163–16174.

[52] Y. Yang, P. Zhang, K. Hu, P. Zhou, Y. Wang, A.H. Asif, X. Duan, H. Sun, S. Wang, Crystallinity and valence states of manganese oxides in Fenton-like polymerization of phenolic pollutants for carbon recycling against degradation, *Appl. Catal. B* 315 (2021), 121593.

[53] X. Xu, L. Li, J. Huang, H. Jin, X. Fang, W. Liu, N. Zhang, H. Wang, X. Wang, Engineering Ni^{3+} cations in NiO lattice at the atomic level by Li^+ doping: the roles of Ni^{3+} and oxygen species for CO oxidation, *ACS Catal.* 8 (9) (2018) 8033–8045.

[54] X. Dong, B. Ren, X. Zhang, X. Liu, Z. Sun, C. Li, Y. Tan, S. Yang, S. Zheng, D. D. Dionysiou, Diatomite supported hierarchical 2D $CoNi_3O_4$ nanoribbons as highly efficient peroxymonosulfate catalyst for atrazine degradation, *Appl. Catal. B* 272 (2020), 118971.

[55] H. Chen, Y. Xu, K. Zhu, H. Zhang, Understanding oxygen-deficient $La_2CuO_{4-\delta}$ perovskite activated peroxymonosulfate for bisphenol A degradation: The role of localized electron within oxygen vacancy, *Appl. Catal. B* 284 (2021), 119732.

[56] Y. Wei, J. Miao, J. Ge, J. Lang, C. Yu, L. Zhang, P.J.J. Alvarez, M. Long, Ultrahigh peroxymonosulfate utilization efficiency over CuO nanosheets via heterogeneous

Cu(III) formation and preferential electron transfer during degradation of phenols, *Environ. Sci. Technol.* 56 (12) (2022) 8984–8992.

[57] H. Lee, H.I. Kim, S. Weon, W. Choi, Y.S. Hwang, J. Seo, C. Lee, J.H. Kim, Activation of persulfates by graphitized nanodiamonds for removal of organic compounds, *Environ. Sci. Technol.* 50 (18) (2016) 10134–10142.

[58] W. Zhao, M. Bajdich, S. Carey, A. Vojvodic, J.K. Nørskov, C.T. Campbell, Water dissociative adsorption on NiO (111): Energetics and structure of the hydroxylated surface, *ACS Catal.* 6 (11) (2016) 7377–7384.

[59] P. Zhang, Y. Yang, X. Duan, Y. Liu, S. Wang, Density functional theory calculations for insight into the heterocatalyst reactivity and mechanism in persulfate-based advanced oxidation reactions, *ACS Catal.* 11 (17) (2021) 11129–11159.

[60] C. Liu, M. Zhang, J. Li, W. Xue, T. Zheng, C. Xia, J. Zeng, Nanoconfinement engineering over hollow multi-shell structured copper towards efficient electrocatalytical C-C coupling, *Angew. Chem. Int. Ed.* 61 (3) (2022) 202113498.

[61] T. Zeng, X. Zhang, S. Wang, H. Niu, Y. Cai, Spatial confinement of a Co₃O₄ catalyst in hollow metal-organic frameworks as a nanoreactor for improved degradation of organic pollutants, *Environ. Sci. Technol.* 49 (4) (2015) 2350–2357.

[62] Y.Z. Ma, H.J. Zhang, R.F. Lin, Y. Ai, K. Lan, L.L. Duan, W.Y. Chen, X.Z. Duan, B. Ma, C.Y. Wang, X.M. Li, D.Y. Zhao, Remodeling nanodroplets into hierarchical mesoporous silica nanoreactors with multiple chambers, *Nat. Commun.* 13 (2022) 6136.

[63] X. Mi, P. Wang, S. Xu, L. Su, H. Zhong, H. Wang, Y. Li, S. Zhan, Almost 100% peroxyomonosulfate conversion to singlet oxygen on single-atom CoN₂₊₂ sites, *Angew. Chem. Int. Ed.* 60 (9) (2021) 4588–4593.

[64] S. Yang, X. Qiu, P. Jin, M. Dzakpasu, X. Wang, Q. Zhang, L. Zhang, L. Yang, D. Ding, W. Wang, K. Wu, MOF-templated synthesis of CoFe₂O₄ nanocrystals and its coupling with peroxyomonosulfate for degradation of bisphenol A, *Chem. Eng. J.* 353 (2018) 329–339.

[65] C. Qi, X. Liu, C. Lin, H. Zhang, X. Li, J. Ma, Activation of peroxymonosulfate by microwave irradiation for degradation of organic contaminants, *Chem. Eng. J.* 315 (2017) 201–209.

[66] A. Jawad, K. Zhan, H. Wang, A. Shahzad, Z. Zeng, J. Wang, X. Zhou, H. Ullah, Z. Chen, Z. Chen, Tuning of persulfate activation from a free radical to a nonradical pathway through the incorporation of non-redox magnesium oxide, *Environ. Sci. Technol.* 54 (4) (2020) 2476–2488.

[67] J. Peng, P. Zhou, H. Zhou, W. Liu, H. Zhang, C. Zhou, L. Lai, Z. Ao, S. Su, B. Lai, Insights into the electron-transfer mechanism of permanganate activation by graphite for enhanced oxidation of sulfamethoxazole, *Environ. Sci. Technol.* 55 (13) (2021) 9189–9198.

[68] W. Ren, C. Cheng, P.H. Shao, X.B. Luo, H. Zhang, S.B. Wang, X.G. Duan, Origins of electron-transfer regime in persulfate-based nonradical oxidation processes, *Environ. Sci. Technol.* 56 (1) (2022) 78–97.